

RADIATION-DRIVEN FOUNTAIN AND ORIGIN OF TORUS AROUND ACTIVE GALACTIC NUCLEI

KEIICHI WADA

Kagoshima University, Kagoshima 890-0065, Japan
Draft version November 8, 2018

ABSTRACT

We propose a plausible mechanism to explain the formation of the so-called “obscuring tori” around active galactic nuclei (AGNs) based on three-dimensional hydrodynamic simulations including radiative feedback from the central source. The X-ray heating and radiation pressure on the gas are explicitly calculated using a ray-tracing method. This radiation feedback drives a “fountain”, that is, a vertical circulation of gas in the central a few to tens parsecs. Interaction between the non-steady outflows and inflows causes the formation of a geometrically thick torus with internal turbulent motion. As a result, the AGN is obscured for a wide range of solid angles. In a quasi-steady state, the opening angles for the column density toward a black hole $< 10^{23} \text{ cm}^{-2}$ are approximately $\pm 30^\circ$ and $\pm 50^\circ$ for AGNs with 10% and 1% Eddington luminosity, respectively. Mass inflows through the torus coexist with the outflow and internal turbulent motion, and the average mass accretion rate to the central parsec region is $2 \times 10^{-4} \sim 10^{-3} M_\odot \text{ yr}^{-1}$; this is about ten times smaller than accretion rate required to maintain the AGN luminosity. This implies that relatively luminous AGN activity is intrinsically intermittent or that there are other mechanisms, such as stellar energy feedback, that enhance the mass accretion to the center.

Subject headings: galaxies: Seyfert – galaxies: starburst – ISM: structure – ISM: molecules – method: numerical

1. INTRODUCTION

The presence of optically thick obscuring tori has been postulated to explain the various observed properties of active galactic nuclei (AGNs), particularly with respect to the two major categories of AGNs, namely, type 1 and type 2 (Antonucci 1993). However, the origin of the optically and geometrically thick material that covers a large solid angle with respect to the AGN and the nature of its three-dimensional structure are still unclear, although its geometry is often schematically described as a “doughnut-shaped” (e.g., Urry & Padovani 1995). In fact, statistical studies of the absorption features of local AGNs suggested have suggested the presence of complex, inhomogeneous obscuring material around the central engine (Shi et al. 2006; Hicks et al. 2009). The clumpy torus model is also consistent with the observed spectral energy distributions (SEDs) (e.g., Nenkova et al. 2002; Elitzur 2006; Levenson et al. 2009; Schartmann et al. 2009; Stalevski et al. 2012). The essential question that then arises is regarding how such an inhomogeneous ‘torus’ is formed and how it attains such a large covering fraction against the energy dissipation of the clumpy medium in the gravitational field of the central black hole.

Numerous theoretical models have been proposed to explain the origin of the obscuring material. On an accretion disk scale the proposed causes include hydromagnetic disk winds (Konigl & Kartje 1994), disk-driven hydromagnetic winds and radiation pressure due to continuum emission from the accretion disk (Keating et al. 2012), and warping of irradiated accretion disks (Armitage & Pringle 1997). Although a parsec-scale dusty torus is observed in some nearby AGNs (Jaffe et al. 2004), the nucleus could be obscured by relatively less dense ISM in the range of 10-100 pc or even by galactic disks themselves (Levenson et al. 2001; Goulding et al. 2012). There are many instances where evidence suggests that most AGNs are associated with circumnuclear starbursts (e.g. Imanishi & Wada 2004; Davies et al. 2007; Hicks et al. 2009; Chen et al. 2009; Imanishi et al. 2011; Diamond-Stanic & Rieke 2012; Woo et al. 2012). It is suggested that the star formation activities drive mass inflow into AGNs, thereby leading to the growth of black holes (see the review by Alexander & Hickox 2011). The nuclear starbursts themselves could inflate the circumnuclear disk and obscure the central source. Wada & Norman (2002) and Wada et al. (2009) have proposed that a clumpy torus-like structure is naturally reproduced due to energy feedback from supernova explosions (SNe) in a disk. In their model, the internal density and temperature of the thick disk are highly inhomogeneous, and the velocity field of the disk is turbulent. The scale height of the disk is determined by the balance between the turbulent energy dissipation and energy input from SNe. More recently, Hopkins et al. (2012) have proposed that 10-pc-scale thick tori can be formed even without the existence of strong stellar energy feedback if gas inflow from kiloparsec scales drives instability in the circumnuclear region.

On a parsec scale or smaller, geometrically and optically thick torus sustained by radiation pressure have been suggested (Krolik & Begelman 1988; Pier & Krolik 1992). Following this model, static solutions of thick disks supported by infrared radiation have been explored by Krolik (2007) and Shi & Krolik (2008). Ohsuga & Umemura (2001) have suggested that static, geometrically thin obscuring walls could be formed by the interplay between the radiation from the nucleus and a ring-like nuclear starburst.

It would be more natural to assume that radiative feedback causes the dynamical evolution of the surrounding ISM rather than static structures. Roth et al. (2012) calculated the net rate of momentum deposition due to the radiation pressure in the surrounding gas and estimated the mass-loss rate by outflow using Monte Carlo radiative transfer calculations. Dorodnitsyn et al. (2012) performed ‘2.5D’ (i.e. basic equations are solved in three dimensions with axisymmetry) radiative hydrodynamic simulations, and they found that an AGN torus can be better described in terms of a radiationally supported flow rather than a quasi-static obscuring torus. Using 2D simulations, Schartmann et al. (2011) studied the evolution of dusty clouds irradiated by the AGN and found that the radiative transfer effect is significant depending on the column density of the clouds.

As is usual in multi-dimensional radiation-hydrodynamic simulations, certain simplifications have been applied in these previous studies, such as assuming flux-limited diffusion approximation and introducing symmetry for the rotational axis and equatorial plane of the AGN. In this study, we examine the effect of the radiation from the central source on the ISM by assuming a different set of simplifications. We performed fully three-dimensional hydrodynamic simulations on scale of a few tens pc around an AGN without introducing any symmetries. We took into account radiative heating and pressure due to “direct radiation” from the central source along rays for all the 256^3 grid cells; however, we ignored the phenomenon of scattering/re-emission. This is a natural extension of our previous three-dimensional hydrodynamic simulations of tens-of-parsec scale tori (Wada & Norman 2002; Wada & Tomisaka 2005; Yamada et al. 2007; Wada et al. 2009), in which self-gravity of the ISM, radiative cooling, SNe, and UV heating were taken into account. Here, we report the first results without SNe feedback. The SED analysis based on the present model will appear elsewhere (Schartmann and Wada, in prep.). In this study, we propose a dynamical process leading to the formation of thick tori, and we examine their structures in a quasi-steady state. Further, we discuss the changes in the column density and the net mass accretion rate depending on the luminosity of the AGN.

2. NUMERICAL METHODS AND MODELS

2.1. Numerical Methods

Based on our three-dimensional, multi-phase hydrodynamic model (Wada et al. 2009), we included the radiative feedback from the central source, i.e., radiation pressure on the dusty gas and the X-ray heating of cold, warm, and hot ionized gas. In contrast to previous analytical and numerical studies of radiation-dominated tori (e.g., Pier & Krolik 1992; Krolik 2007; Shi & Krolik 2008; Diamond-Stanic & Rieke 2012; Dorodnitsyn et al. 2011, 2012), we assume neither dynamical equilibrium nor geometrical symmetry. Here, we solve fully three-dimensional hydrodynamic equations, accounting for radiative feedback processes from the central source using a ray-tracing method. In a manner similar to the approach by Wada & Norman (2002), we account for self-gravity of the gas, radiative cooling for $20 \text{ K} < T_{gas} < 10^8 \text{ K}$, uniform UV radiation for photoelectric heating and H_2 formation/destruction (Wada et al. 2009); however, we do not include the effect of supernova feedback in this study, in order to clarify the effect of the radiation feedback only. We plan to investigate the effects of supernova in the circumnuclear starburst in a future study.

We use a numerical code based on Eulerian hydrodynamics with a uniform grid (Wada & Norman 2001; Wada 2001; Wada et al. 2009). We solve the following equations numerically to simulate the three-dimensional evolution of a rotating gas disk in a fixed spherical gravitational potential under the influence of radiation from the central source.

$$\partial\rho/\partial t + \nabla \cdot (\rho\mathbf{v}) = 0, \quad (1)$$

$$\partial(\rho\mathbf{v})/\partial t + (\mathbf{v} \cdot \nabla)\mathbf{v} + \nabla p = -\rho(\nabla\Phi + \mathbf{f}_{rad}^r), \quad (2)$$

$$\partial(\rho E)/\partial t + \nabla \cdot [(\rho E + p)\mathbf{v}] - \rho\mathbf{v} \cdot \nabla\Phi = \rho\Gamma_{UV}(G_0) + \rho\Gamma_X - \rho^2\Lambda(T_{gas}, f_{\text{H}_2}, G_0), \quad (3)$$

$$\nabla^2\Phi_{sg} = 4\pi G\rho, \quad (4)$$

where $\Phi(\mathbf{x}) \equiv \Phi_{\text{ext}}(r) + \Phi_{\text{BH}}(r) + \Phi_{\text{sg}}(\mathbf{x})$; ρ, p, \mathbf{v} denote the density, pressure, and velocity of the gas, and the specific total energy $E \equiv |\mathbf{v}|^2/2 + p/(\gamma - 1)\rho$, with $\gamma = 5/3$. We assume a time-independent external potential $\Phi_{\text{ext}}(r) \equiv -(27/4)^{1/2}[v_1^2/(r^2 + a_1^2)^{1/2} + v_2^2/(r^2 + a_2^2)^{1/2}]$, where $a_1 = 100 \text{ pc}$, $a_2 = 2.5 \text{ kpc}$, $v_1 = 147 \text{ km s}^{-1}$, $v_2 = 147 \text{ km s}^{-1}$, and $\Phi_{\text{BH}}(r) \equiv -GM_{\text{BH}}/(r^2 + b^2)^{1/2}$, where $M_{\text{BH}} = 1.3 \times 10^7 M_{\odot}$ (see Fig. 1 in Wada et al. (2009) for the rotation curve). The potential caused by the black hole (BH) is smoothed within $r \sim b = 4\delta$, where δ denotes the minimum grid size ($= 0.25 \text{ pc}$), in order to avoid too small time steps around the BH. In the central grid cells at $r < 2\delta$, physical quantities remains constant.

We solve the hydrodynamic part of the basic equations using AUSM (Advection Upstream Splitting Method)(Liou & Steffen 1993). We use 256^3 grid points. The uniform Cartesian grid covers a 64^3 pc^3 region around the galactic center (i.e. the spatial resolution is 0.25 pc). The Poisson equation, eq.(4) is solved to calculate the self-gravity of the gas using the fast Fourier transform and the convolution method with 512^3 grid points along with a periodic Green’s function. We solve the non-equilibrium chemistry of hydrogen molecules along with the hydrodynamic equations (Wada et al. 2009).

We consider the radial component of the radiation pressure:

$$\mathbf{f}_{rad}^r = \int \frac{\chi_{\nu}\mathbf{F}_{\nu}^r}{c} d\nu, \quad (5)$$

where χ_{ν} denotes the total mass extinction coefficient due to dust absorption and Thomson scattering, i.e. $\chi_{\nu} \equiv$

$\chi_{dust,\nu} + \chi_T$. The radial component of the flux at the radius r , \mathbf{F}_ν^r is

$$\mathbf{F}_\nu^r \equiv \frac{L_\nu(\theta)e^{-\tau_\nu}}{4\pi r^2} \mathbf{e}_r, \quad (6)$$

where $\tau_\nu = \int \chi_\nu \rho ds$.

The only explicit radiation source used here is an accretion disk whose size is five orders of magnitude smaller than the grid size in the present calculations. Therefore we assumed that radiation is emitted from a point source. However, the radiation flux originating from the accretion disk is not necessarily spherically symmetric (e.g. Netzer 1987). In our study, we simply assume emission from a thin accretion disk without considering the limb darkening effect, i.e., $L_\nu \equiv 2L_{AGN}|\cos\theta|$, where θ denotes the angle from the rotational axis (z -axis) (see also discussion in §4).

In the simulations, we considered the radial component of the flux \mathbf{f}_{rad}^r only for the radiative heating and pressure. This approximation is not necessarily correct especially with respect to optically thick dusty gas around the central few parsecs; however, beyond this region, the acceleration of the gas due to strong X-rays can be expected to be radial. Even for the central region spanning a few parsecs, Roth et al. (2012) showed that the gas acceleration is nearly radial using three-dimensional Monte Carlo radiative transfer calculations. It is noteworthy that since the hydrodynamics is calculated in a fully three-dimensional manner, the radiative acceleration may contribute to gas dynamics along any direction. Therefore the resultant density and velocity structures could be very different from the symmetric ones (cf. Ohsuga & Umemura 2001). The optical depth τ_ν is calculated at every time step along a ray from the central source at each grid point, i.e. 256^3 rays are used in the computational box.

In the energy equation (eq. (3)), we use a cooling function based on a radiative transfer model of photodissociation regions (Meijerink & Spaans 2005), denoted as $\Lambda(T_g, f_{H_2}, G_0)$, assuming solar metallicity, which is a function of the molecular gas fraction f_{H_2} and the intensity of far ultraviolet (FUV), G_0 , (Wada et al. 2009). The radiative cooling rate below $\simeq 10^4$ K is self-consistently modified depending on f_{H_2} , which is determined for each grid cell. We include the effect of heating due to the photoelectric effect, Γ_{UV} . We assume a uniform FUV radiation field, with the Habing unit $G_0 = 1000$, originating in the star-forming regions in the central several tens parsecs. In reality, both the density field and distribution of massive stars should not be uniform, and G_0 should have a large dispersion with some radial dependence. However, the FUV radiation affects the chemistry of the ISM (mostly distribution of molecular clouds) although this does not significantly alter the dynamics of the circumnuclear ISM (Wada et al. 2009). The effects of the non-uniform radiation field with multiple sources on the gas dynamics is an important problem, but it is beyond the scope of this paper.

The temperature of the interstellar dust, T_{dust} , at a given position irradiated by the central source is calculated by assuming thermal equilibrium (e.g. Nenkova et al. 2008), and if $T_{dust} > 1500$ K, we assume that the dust is sublimate. Here we assume that the ISM in the central tens parsecs is optically thin with respect to the re-emission from the host dust. The SED of the AGN and the dust absorption cross section are taken from Laor & Draine (1993). We use a standard galactic dust model, which is the same as that used by Schartmann et al. (2010), with eight logarithmic frequency bins between $0.001 \mu m$ and $100 \mu m$.

The effects hard X-ray on the thermal and chemical structures of the ISM are significant in the region spanning subparsec distances to tens of parsecs (Pérez-Beaupuits et al. 2011). Further, X-ray heating may be essential for galactic scale feedback (Hambrick et al. 2011). Here, we consider heating by the X-ray, i.e. interactions between the high energy secondary electrons and thermal electrons (Coulomb heating), and H_2 ionizing heating in the warm and cold gas (Maloney, Hollenbach, & Tielens 1996; Meijerink & Spaans 2005). The Coulomb heating rate $\Gamma_{X,c}$ for the gas with the number density n is given by

$$\Gamma_{X,c} = \eta n H_X, \quad (7)$$

where η denotes the heating efficiency (Dalgarno et al. 1999; Meijerink & Spaans 2005), and the X-ray energy deposition rate $H_X = 3.8 \times 10^{-25} \xi$ ergs s^{-1} and the ionizing parameter $\xi = 4\pi F_X/n = L_X e^{-\int \tau_\nu d\nu}/nr^2$, with $L_X = 0.1L_{AGN}$. For optically thin hot gas with $T \gtrsim 10^4 K$, the effects of Compton heating and X-ray photoionization heating are considered, and the net heating rate (Blondin 1994) is approximately

$$\Gamma_{X,h} = 8.9 \times 10^{-36} \xi (T_X - 4T) + 1.5 \times 10^{-21} \xi^{1/4} T^{-1/2} (1 - T/T_X) \text{ erg s}^{-1} \text{ cm}^3, \quad (8)$$

with the characteristic temperature of the X-ray radiation, $T_X = 10^8$ K.

2.2. Initial conditions and model parameters

In order to prepare a quasi-steady initial condition without radiation feedback, we first run a model of an axisymmetric and rotationally supported thin disk with a uniform density profile (thickness of 2.5 pc) and a total gas mass of $M_g = 6.68 \times 10^6 M_\odot$. Random density fluctuations, which are less than 1% of the unperturbed values, are added to the initial gas disk. After $t \sim 1.7$ Myr, the thin disk settles in a flared shape with the total mass $6.64 \times 10^6 M_\odot$. Since we allow outflows from the computational boundaries, the total gas mass decreases during the evolution.

A free parameter in the present simulations is the luminosity of the AGN. Here, we explore models with two different Eddington ratios $L_{AGN}/L_E = 0.1$ and 0.01 , where the Eddington luminosity $L_E \equiv 4\pi G c m_p M_{BH}/\sigma_T$. In each model, L_{AGN} stays constant during calculations, i.e. ~ 3 Myrs¹.

¹ The numerical calculations were carried out on the NEC SX-9 (16 vector processors/1 TB memory/1.6 TFlops) at the National

3. RESULTS

3.1. Onset of Thick Torus

Figure 1 shows the onset of biconical outflows, cavities, and thick disk after the radiation from the central source is initiated. Radiation-driven outflows start forming in the inner region, and subsequently propagate outward. At $t = 1.986$ Myr, “back-flows” toward the disk plane appear outside the biconical outflows. These accretion flows interact with the disk, thereby leading to the formation of a geometrically thick disk that has a clear boundary with $\rho \sim 10^2 M_\odot \text{ pc}^{-3}$ (Fig. 1).

The interactions of vertical flows with opposite directions are more clearly seen in Fig. 2 ($t = 2.146$ Myr), which shows the distribution of v_z . There are several contact surfaces between upward and downward flows. As a result, turbulent motions that support the thick geometrical structure of the disk are generated. The complicated distribution of flows in the thick disk is also seen in the velocity field at the equatorial plane (left panel of Fig. 2).

The downward flows can be naturally expected due to the balance between radiation pressure and the gravity. The ratio between the radiation pressure for the dusty gas and the gravity due to the central BH is

$$\frac{f_{rad}}{f_{gravi}} = \frac{L_{AGN} \chi_d |\cos \theta|}{4\pi G c M_{BH}} e^{-\tau_d}, \quad (9)$$

where τ_d denotes the optical depth for the dusty gas at a given point. Suppose that the gas density is a function of z , e.g., $n(z) = N_{col}/\sqrt{2\pi} h e^{-z^2/2h^2}$. Fig. 3 shows how the radiation-pressure-dominated region and gravity-dominated region are distributed around the AGN for the given gas density. Here, we assume the dust-to-gas mass ratio of 0.03 (Ohsuga & Umemura 2001), $L_{AGN} = 10^{44} \text{ erg s}^{-1}$, dust extinction coefficient $\chi_d = 10^5 \text{ cm}^2 \text{ g}^{-1}$, and the gas density at $z = 0$ as $n_0 = 1000 \text{ cm}^{-3}$. The four curves represent the condition $f_{rad}/f_{gravi} = 1$, with the vertical extent of the gas $h = 4, 6, 8,$ and 10 pc , for which radiation pressure dominates in the inner side of the curve, therefore outflows are expected. On the other hand, the radiation pressure cannot prevent gas accretion outside the critical lines. In fact, accretion flows appear in the gravity-dominated domain as seen in Figs. 1 and 2. Moreover, since the critical lines dividing the two domains are not purely radial (Fig. 3), outflows with large angles from the z -axis may collide with the boundary of the cavity. This pushes the boundaries of the outflow outward, and the gases in the outflows change their directions and fall towards the center as indicated by the velocity vectors in Fig. 2. This also causes the biconical cavities to become non-steady, and the vertical circulation of the flow, or the “fountain” of gas, circulates around the AGN on a scale of 10 pc . The kinetic energy of this circulating flow is partially used to generate the random motion in the disk and maintain its thickness. In other words, both radiation energy and gravity are the cause of origin of the internal turbulent motion in the disk².

3.2. Structures and Dynamics in Quasi-steady State

Figure 4 shows that the density structures in a quasi-steady states differ depending on the luminosity of the central source. Here “quasi-steady” means that the global morphology has reached an approximately steady state; that is the phase diagram of the gas (Fig. 6) does not significantly change after this point. The accretion rates to the central region are also approximately constant. This is achieved roughly after $t = 3.0 - 3.5$ Myr (Fig. 9). Note that since the duration of the present simulation is much shorter than the accretion time scale ($\sim 10^9$ Myr), the ‘quasi-steady’ does not necessary mean the long-term stability.

In the more luminous model ($L_{AGN}/L_{Edd} = 0.1$, upper panels), inhomogeneous outflows with $\rho \sim 0.1 - 1 M_\odot \text{ pc}^{-3}$ and velocity of $\sim 100 \text{ km s}^{-1}$ are formed, and diffuse gas ($\rho \sim 0.1 M_\odot \text{ pc}^{-3}$) extends for over 20 pc above the equatorial plane. On the other hand, diffuse and relatively stable outflows with $\rho \sim 10^{-2} M_\odot \text{ pc}^{-3}$ or less are formed in the less luminous model with $L_{AGN}/L_{Edd} = 0.01$. The gas temperature distributions of the two models (Fig. 5) show that dense spiral arms and clumps in the equatorial plane exhibit a temperature of less than 1000 K , in contrast to the “warm” ($\sim 10^4 - 5 \text{ K}$) torus. In the less luminous AGN model, an increased number of hot gas ($\gtrsim 10^6 \text{ K}$) regions appear in the biconical outflow. This is because the radiative cooling is less effective due to reduced gas density in the region, and as a consequence, the X-ray is not attenuated.

Figure 6 shows the effects of the radiative feedback on the phases of the gas. The dominant phase is the one around $T_{gas} \sim 8000 \text{ K}$. The dense and cold gas ($\rho > 10^2 M_\odot \text{ pc}^{-3}$ and $T_{gas} < 1000 \text{ K}$) is not affected by the radiative feedback. The X-ray heating produces warm ($T_{gas} < 1000 \text{ K}$) gas in the outer regions (i.e., high latitude) of the thick disk, as is expected from the XDR model (Pérez-Beaupuits et al. 2011). Shock-heated gas with a temperature of several 10^4 K also appears in the same density region.

The structure of the torus does not show perfect symmetry for the rotational axis and the equatorial plane. Figure 7 shows four different vertical slices of density around the rotational axis of the model shown in the upper panel of Fig. 4. The diffuse part of torus ($\rho \sim 10^2$) is slightly tilted, thereby indicating that the outlying region of the disk is not completely settled. The shell-like outflows also show asymmetric distributions. It is interesting to note that these structures are caused by interactions between the radiation from the central symmetric source and the surrounding

Astronomical Observatory of Japan and Cyberscience Center, Tohoku University. A single typical run for 3 Myr takes approximately 120 CPU hours.

² In a self-gravitating, multi-phase gas disk, gravitational and thermal instabilities themselves can generate and maintain turbulent motion (Wada et al. 2002). In the present model, random motions of the high-density gas near the equatorial plane ($z \sim 0$) are dominated by this gravity-driven turbulence. However, the random motions along the vertical direction in the less dense gas in the thick disk are not driven by gravitational instability.

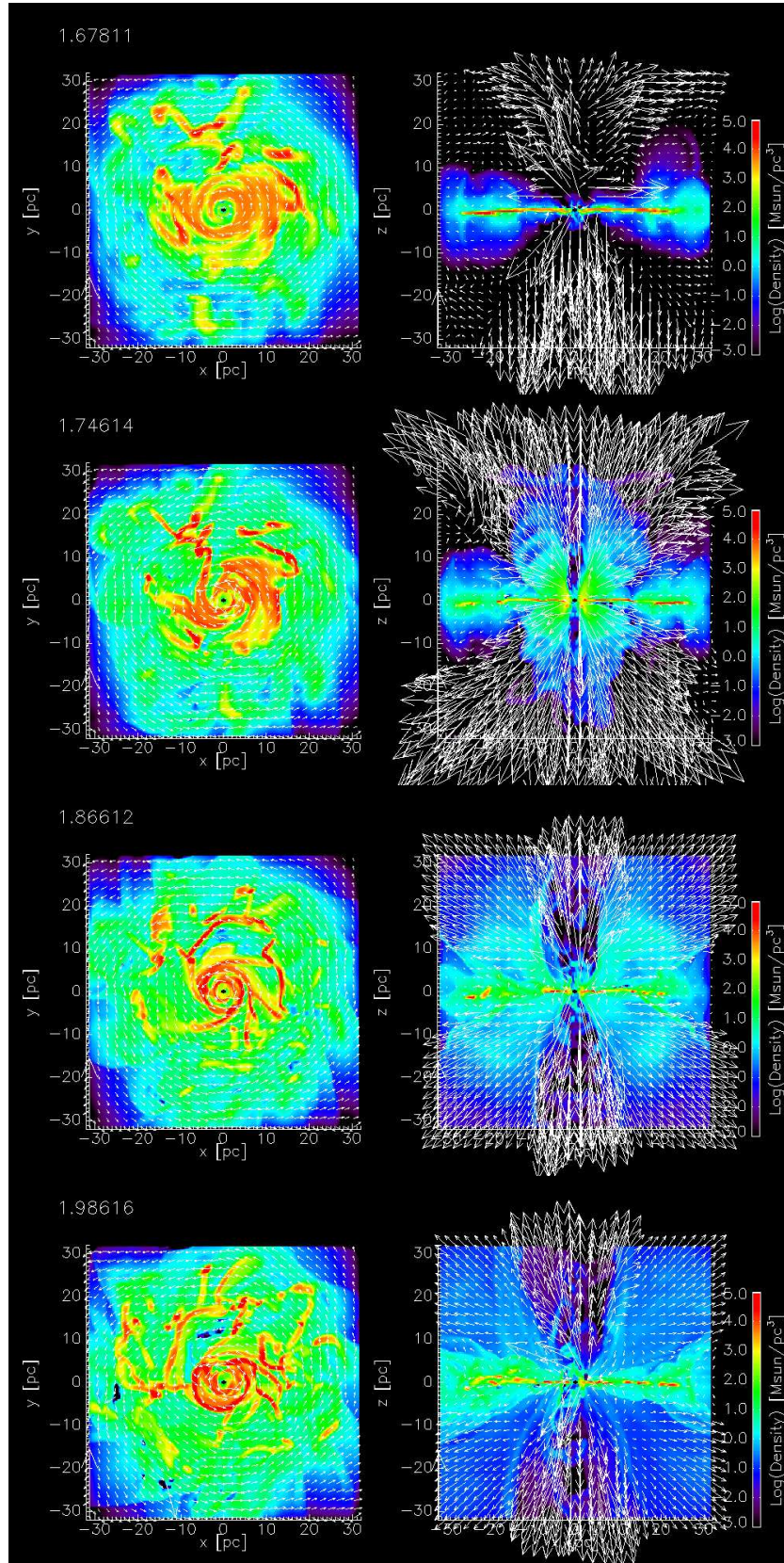


FIG. 1.— Initial evolution of radiation-driven outflow and onset of thick disk in a model with $L_{\text{AGN}}/L_{\text{Edd}} = 0.1$. The vertical slices represent the x - z planes. Arrows represent gas velocity (a unit vector of 500 km s^{-1} is shown as reference along the y -axis.)

inhomogeneous gas, thereby demonstrating importance of the three-dimensional treatment of radiation hydrodynamics in understanding the structure of AGN.

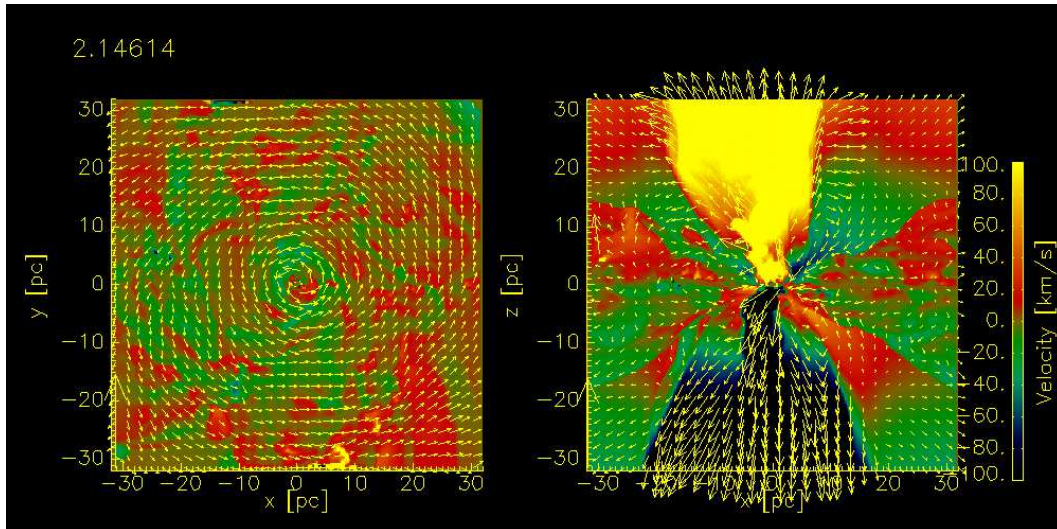


FIG. 2.— Observed z -component of velocity at $t = 2.15$ Myr ($L_{AGN}/L_E = 0.1$). The vertical slice indicates the x - z plane. The downward flows (i.e., flow heading to the equatorial plane) appear outside the region of the biconical outflow, and these flows interact with the opposite directed flows, which are represented by the regions indicated in green/blue and red/yellow. The upward and downward flows coexist and generate turbulent motions in the equatorial plane (left panel) as well as in the vertical direction.

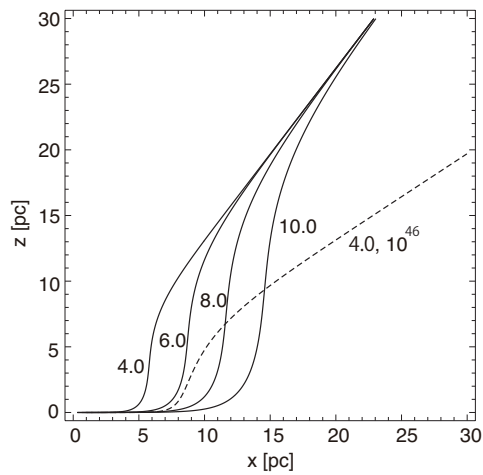


FIG. 3.— Critical lines between radiation-pressure dominant and gravity dominant regions for gas disk with different vertical extensions, represented by $n(z) = n_0/(\sqrt{2\pi}h)e^{-z^2/2h^2}$ with $h = 4, 6, 8,$ and 10 pc. The dashed line indicates the critical line for $h = 4$ pc and $L_{AGN} = 10^{46}$ erg s $^{-1}$, which is 100 times that for the other cases.

Obscuration due to the vertically extended gas in the central region over tens of parsecs and how it differs between models are shown in Fig. 8, which shows the plot of the column density toward the central BH as a function of the viewing angle. If there is no radiation from the central source, the opening angle for $N \leq 10^{23}$ cm $^{-2}$ is approximately 140° . The radiation feedback causes the thickness of the disk to increase, and the opening angles are approximately 60° and 100° for $L_{AGN}/L_E = 0.1$ and 0.01 , respectively. It is noteworthy that the column density does not only depend on the viewing angle, but also on the azimuthal angles. The column density varies by a factor of ten or more for a given viewing angle, thereby indicating the internal inhomogeneous structure of the disk. The structure of the disk is similar to that generated by supernova explosions (Wada & Norman 2002; Wada et al. 2009). However, the present simulations imply that the geometrically and optically thick torus can be naturally formed due to gravitational energy in the central part with the aid of the radiation feedback in the case of the AGNs with low Eddington ratios.

The radiation pressure caused by the central source usually has “negative” effect on the mass accretion toward the center; however, our results indicate that mass accretion is not terminated by radiative feedback. Figure 9 shows the time evolution of the mass of the two models in four radial bins. The lower luminosity model ($L_{AGN}/L_{Edd} = 0.01$) shows continuous *net* mass accretion in the central 8-pc region, and there is almost no net inflow beyond $r \sim 4$ pc. The mass accretion in the central part is caused by gravitational torque due to the non-axisymmetric features near the equatorial plane of the central part of the disk (Fig. 1).³

³ The amount of the angular momentum transfer during one rotational period by m -armed spiral density waves is roughly proportional

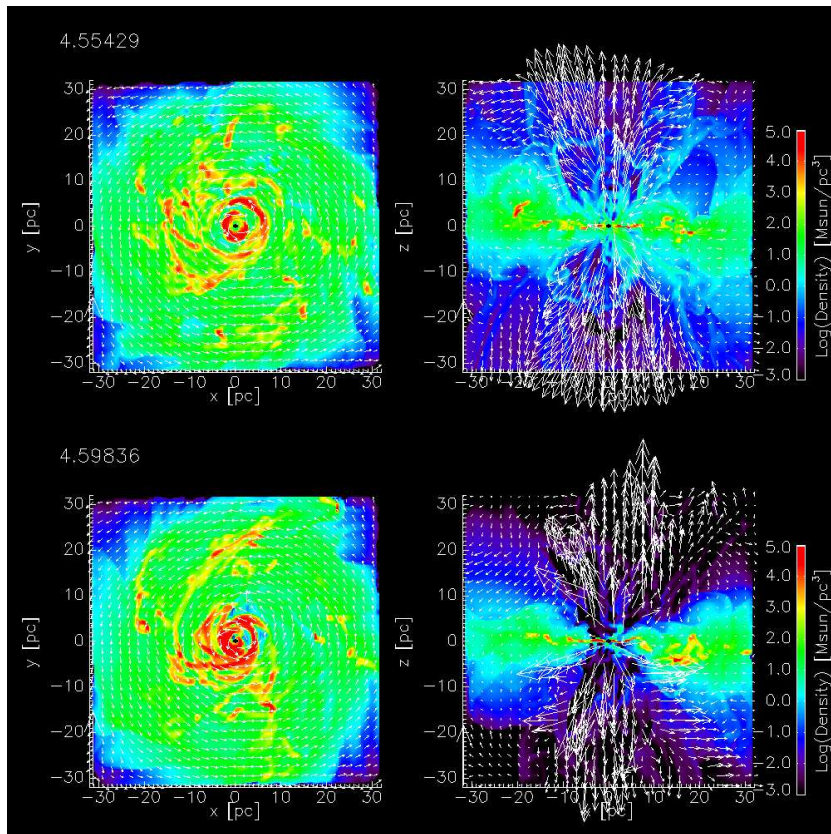


FIG. 4.— Gas density in quasi-steady state of two models: (top) $L_{AGN}/L_E = 0.1$ at $t = 4.55$ Myr and (bottom) $L_{AGN}/L_E = 0.01$ at $t = 4.59$ Myr. The vertical slices indicate the x - z planes.

The accretion rate to the central parsec increases with decreasing AGN luminosity: $\dot{M} = 1.7 \times 10^{-3} M_{\odot} \text{ yr}^{-1}$ and $\dot{M} = 1.3 \times 10^{-4} M_{\odot} \text{ yr}^{-1}$ for $L_{AGN}/L_E = 0.01$ and 0.1 , respectively. For $L_{AGN} = 0.1 L_E$, the net accretion rate is one order of magnitude *smaller* than the accretion rate required to constant AGN luminosity; the AGN luminosity is assumed to be constant during the calculations provided that the energy conversion efficiency is 0.1. On the other hand, the observed accretion rate in the low luminosity AGN model is comparable to that required for the luminosity of the source. These results may suggest that luminous AGNs are intermittent, and their luminosity is not instantaneously determined by mass inflow from $r \sim 1$ pc.

4. CONCLUSION AND DISCUSSION

In our study, we showed that a geometrically and optically thick torus can be naturally formed in the central region extending tens parsecs around a low luminosity AGN. We found that radiation drives a “fountain” of gas, i.e. vertical circulation, and this also naturally produces a thick, turbulent, and inhomogeneous disk that resembles a torus. The opening angle of the torus for $N < 10^{23} \text{ cm}^{-3}$ is $60 - 100^\circ$ for $L_{AGN} = 0.1 - 0.01 L_E$, in contrast to 140° for the model without radiative feedback. The average accretion rate to the central parsec region is larger in a less luminous AGN; however, this accretion rate is insufficient to maintain the AGN luminosity over several Myrs. These results imply that the AGN luminosity and structure of the surrounding ISM alternate between an active phase (high luminosity and a torus with a small opening angle) and inactive phase (low luminosity and a torus with a large opening angle). For thick tori (Fig. 4) to maintained their structures for several million years or longer, there should be other mechanisms to enhance the accretion rate, such as supernova-driven turbulence (Wada & Norman 2002; Wada et al. 2009), stellar mass loss (Schartmann et al. 2010), turbulence drives by galactic inflows (Hopkins et al. 2012) and radiation drag (Kawakatu & Umemura 2002). In fact, recent observations suggest a tight correlation between star formation rate and the Eddington ratio of the central BH (Chen et al. 2009).

Figure 8 shows that the covering fraction of the central source is smaller in AGNs with lower luminosity. This is because more mass can be ejected from the central region to higher latitudes, and as a result, the radiation from the AGN is self-obscured. Therefore, the radiation-driven outflows appear only in a small solid angle around the rotational axis, as explained in §3.1 and illustrated in Fig. 3. This means that more luminous AGNs are obscured over larger solid angles, although this may appear inconsistent with the observed “receding torus” (Lawrence 1991; Ueda et al. 2003). For example, Hasinger (2008) studied 1290 AGNs and found that the absorbed fraction *decreases* with X-ray luminosity in the range of $L_X = 10^{42-46} \text{ erg s}^{-1}$. However, it is to be noted that the AGNs explored in the present simulation

to $\pi \tan \theta_i A_m^2 / m$ (e.g. Binney & Tremaine 2008), where A_m is a ratio of the amplitude of the spiral to the average density, and θ_i is the pitch angle of the spiral. For non-linearly developed spiral waves (i.e. $A_m \gtrsim 1$) with $\tan \theta_i \sim 0.1$, $m \sim 1$, about 3% of the initial angular momentum of the disk is transferred in a rotational period.

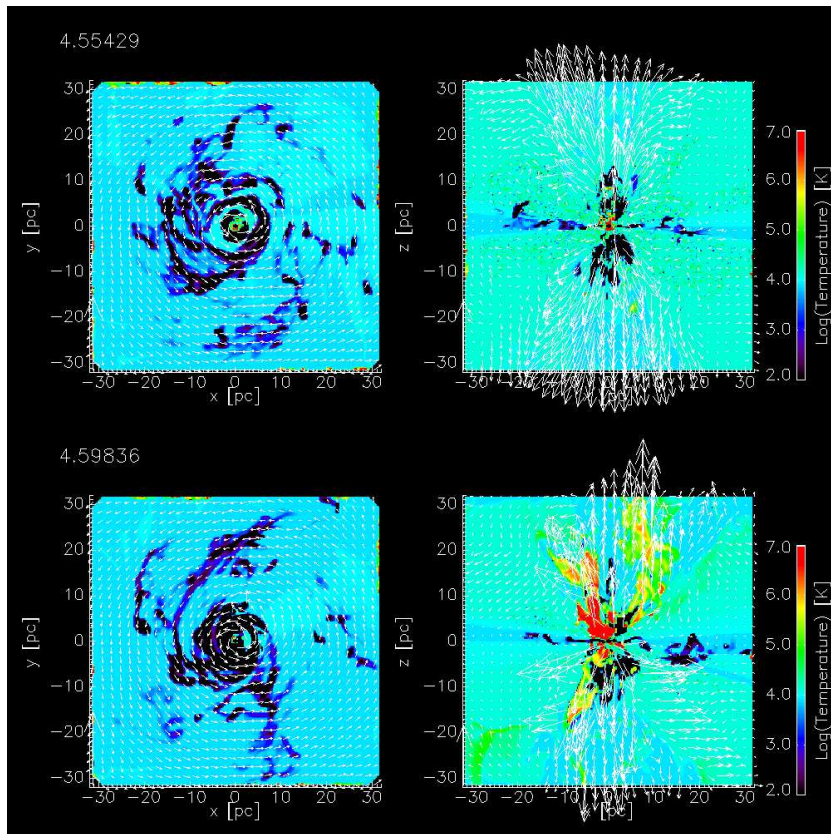


FIG. 5.— Gas temperature in quasi-steady state of two models: (top) $L_{\text{AGN}}/L_E = 0.1$ at $t = 4.55$ Myr and (bottom) $L_{\text{AGN}}/L_E = 0.01$ at $t = 4.59$ Myr. The vertical slices indicate the x - z planes.

have relatively low luminosity, i.e., in the range of $L_X = 10^{42-43}$ erg s $^{-1}$. In this small luminosity range, the structure of the torus does not vary significantly, especially for higher values of column density ($N > 10^{24}$ cm $^{-2}$). For a central source that is 100 times brighter, the radiation-dominant region is considerably larger, as shown by the dashed line in Fig. 3, and therefore, we can expect a larger opening angle for this case. More recently, Lu et al. (2010) have reported results that are significantly different from those of previous studies; in their SDSS/FIRST survey, they found that the type-1 fraction exhibits a constant of 20% in the [O III] 5007 luminosity range of $40.7 < \log(L_{[\text{O III}]})/\text{erg s}^{-1} < 43.5$. They also found that the type-1 fraction is independent of the Eddington ratio for its value between 0.01 and 1, if only high density ($> 10 M_\odot \text{ pc}^{-3}$) gas in the torus contributes to the obscuration; this is also the case as seen in Fig. 4.

Further, this study shows that the global structures of the torus and outflows are not static, and there is never a perfect symmetry in terms of the equatorial plane and the rotation axis (Fig. 7), even if we assume the presence of angle-dependent, axisymmetric flux from the central source. The opening angle of the torus and other structures could be affected by the choice of the central radiation source. In this study, we assumed a thin accretion disk; however, recent two-dimensional radiation-magnetohydrodynamic simulations have shown that geometrically thick and radiatively inefficient accretion flows associated with outflows are formed depending on the central gas density (Ohsuga & Mineshige 2011). In this case, the radiation flux is collimated around the rotation axis, and the effect of the radiation on the disk might be less than that observed in the models used in this study. Even for a thin accretion disk, the rotational axis is not necessarily aligned to the galactic rotational axis. This causes anisotropic illumination of the ISM, and this misalignment could also affect the occultation of the central source by the torus (see also Kawaguchi & Mori 2011). Consequently, we can expect the formation of more such anisotropic structures of the torus and outflows in such cases. This can be confirmed by high-resolution observations of nuclear active galaxies associated with molecular outflows, such as NGC 1377 (Aalto et al. 2012) and by ALMA in the near future.

The author is grateful to M. Schartmann for providing the dust absorption tables and also for his helpful comments regarding the draft. We also thank M. Spaans and the anonymous referee for many valuable comments. The numerical computations presented in this paper were carried out on the NEC SX-9 in the Center for Computational Astrophysics, NAOJ and Cyberscience Center, Tohoku University. The author thanks N. Horiuchi, Y. Sakaguchi, and the NEC Corporation for optimizing the code for the SX-9. This work is partly supported by Grant-in-Aid for Scientific Research (C) 23540267.

REFERENCES

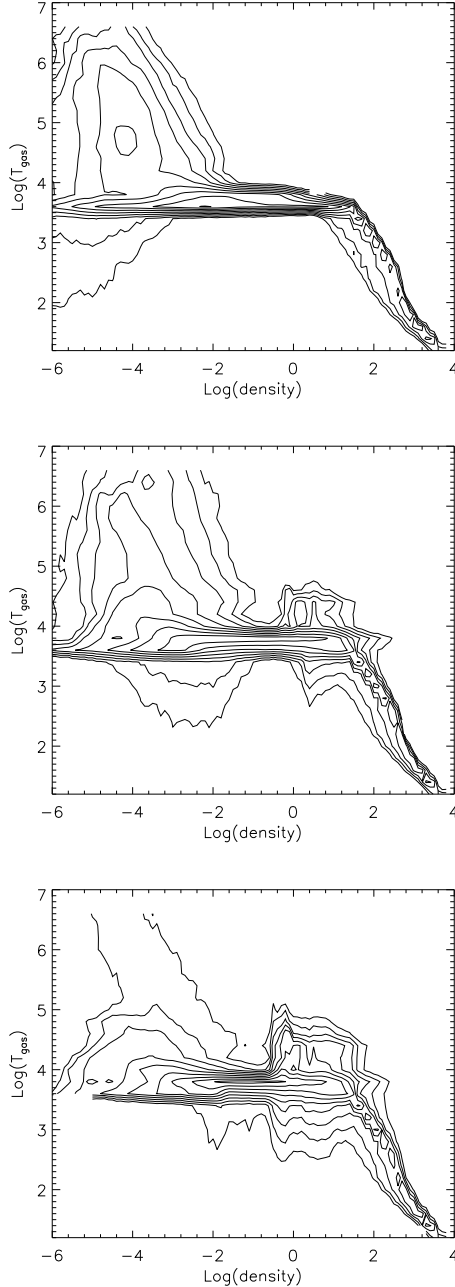


FIG. 6.— Volumes in gas density [$M_{\odot} \text{pc}^{-3}$] and temperature [K]. (top) no radiation feedback, (middle) $L_{AGN}/L_E = 0.01$, (bottom) $L_{AGN}/L_E = 0.1$.

- Antonucci, R. 1993, *ARA&A*, 31, 473
 Armitage, P. J. & Pringle, J. E. 1997, *ApJ*, 488, L47
 Binney, J., Tremaine, S., “Galactic Dynamics (2nd. edition)”, Princeton University Press, Princeton (2008), p.479
 Blondin, J. M. 1994, *ApJ*, 435, 756
 Chen, Y.-M., Wang, J.-M., Yan, C.-S., Hu, C., & Zhang, S. 2009, *ApJ*, 695, L130
 Dorodnitsyn, A., Kallman, T., & Bisnovatyi-Kogan, G. S. 2012, *ApJ*, 747, 8
 Dorodnitsyn, A., Bisnovatyi-Kogan, G. S., & Kallman, T. 2011, *ApJ*, 741, 29
 Diamond-Stanic, A. M., & Rieke, G. H. 2012, *ApJ*, 746, 168
 Dalgarno, A., Yan, M., & Liu, W. 1999, *ApJS*, 125, 237
 Davies, R. I., Sánchez, F. M., Genzel, R., Tacconi, L. J., Hicks, E. K. S., Friedrich, S., & Sternberg, A. 2007, *ApJ*, 671, 1388
 Eitzur, M. 2006, *New Astronomy Review*, 50, 728
 Goulding, A. D., Alexander, D. M., Bauer, F. E., et al. 2012, arXiv:1205.1800
 Hambrick, D. C., Ostriker, J. P., Naab, T., & Johansson, P. H. 2011, *ApJ*, 738, 16
 Hasinger, G. 2008, *A&A*, 490, 905
 Hicks, E. K. S., Davies, R. I., Malkan, M. A., Genzel, R., Tacconi, L. J., Sánchez, F. M., & Sternberg, A. 2009, *ApJ*, 696, 448
 Hopkins, P. F., Hayward, C. C., Narayanan, D., & Hernquist, L. 2012, *MNRAS*, 420, 320
 Imanishi, M., Ichikawa, K., Takeuchi, T., et al. 2011, *PASJ*, 63, 447
 Imanishi, M., & Wada, K. 2004, *ApJ*, 617, 214
 Jaffe, W., et al. 2004, *Nature*, 429, 47
 Keating, S. K., Everett, J. E., Gallagher, S. C., & Deo, R. P. 2012, *ApJ*, 749, 32
 Kawakatu, N., & Umemura, M. 2002, *MNRAS*, 329, 572

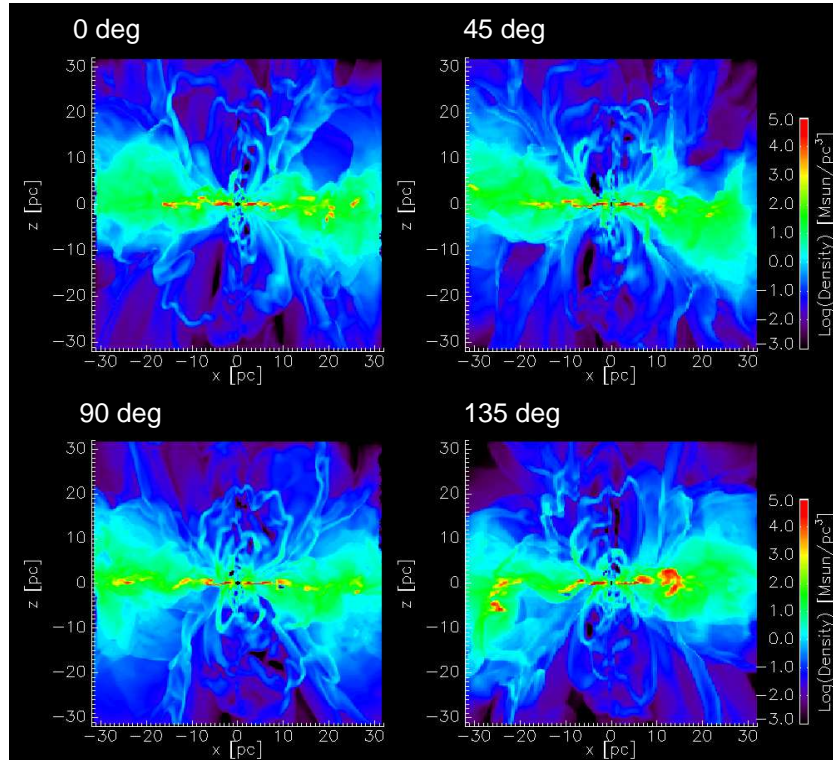


FIG. 7.— Azimuthal change of gas density distribution of model with $L_{AGN}/L_E = 0.1$ at $t = 4.59$ Myr. In each panel, x-axis is inclined at 0° , 45° , 90° , and 135° to the original x -axis of the computational box.

- Kawaguchi, T., & Mori, M. 2011, *ApJ*, 737, 105
 Konigl, A., & Kartje, J. F. 1994, *ApJ*, 434, 446
 Krolik, J. H. 2007, *ApJ*, 661, 52
 Krolik, J. H. & Begelman, M. C. 1988, *ApJ*, 329, 702
 Laor, A., & Draine, B. T. 1993, *ApJ*, 402, 441
 Lawrence, A. 1991, *MNRAS*, 252, 586
 Levenson, N. A., Weaver, K. A., & Heckman, T. M. 2001, *ApJS*, 133, 269
 Levenson, N. A., Radomski, J. T., Packham, C., et al. 2009, *ApJ*, 703, 390
 Liou, M., Steffen, C., 1993, *J. Comp. Phys.*, 107, 23
 Lu, Y., Wang, T.-G., Dong, X.-B., & Zhou, H.-Y. 2010, *MNRAS*, 404, 1761
 Maloney, P. R., Hollenbach, D. J., & Tielens, A. G. G. M. 1996, *ApJ*, 466, 561
 Meijerink, R., & Spaans, M. 2005, *A&A*, 436, 397
 Nenkova, M., Ivezić, Ž., & Elitzur, M. 2002, *ApJ*, 570, L9
 Nenkova, M., Sirocky, M. M., Ivezić, Ž., & Elitzur, M. 2008, *ApJ*, 685, 147
 Netzer, H. 1987, *MNRAS*, 225, 55
 Ohsuga, K. & Umemura, M. 2001, *A&A*, 371, 890
 Ohsuga, K., & Mineshige, S. 2011, *ApJ*, 736, 2
 Pérez-Beaupuits, J. P., Wada, K., & Spaans, M. 2011, *ApJ*, 730, 48
 Pier, E. A. & Krolik, J. H. 1992, *ApJ*, 399, L23
 Pier, E. A., & Krolik, J. H. 1993, *ApJ*, 418, 673
 Roth, N., Kasen, D., Hopkins, P. F., & Quataert, E. 2012, arXiv:1204.0063
 Shi, Y., Rieke, G. H., Hines, D. C., et al. 2006, *ApJ*, 653, 127
 Shi, J., & Krolik, J. H. 2008, *ApJ*, 679, 1018
 Schartmann, M., Meisenheimer, K., Klahr, H., Camenzind, M., Wolf, S., & Henning, T. 2009, *MNRAS*, 393, 759
 Schartmann, M., Burkert, A., Krause, M., et al. 2010, *MNRAS*, 403, 1801
 Schartmann, M., Krause, M., & Burkert, A. 2011, *MNRAS*, 415, 741
 Stalevski, M., Fritz, J., Baes, M., Nakos, T., & Popović, L. Č. 2012, *MNRAS*, 420, 2756
 Urry, C. M., & Padovani, P. 1995, *PASP*, 107, 803
 Ueda, Y., Akiyama, M., Ohta, K., & Miyaji, T. 2003, *ApJ*, 598, 886
 Wada, K. 2001, *ApJ*, 559, L41
 Wada, K., Meurer, G., & Norman, C. A. 2002, *ApJ*, 577, 197
 Wada, K. & Norman, C. A. 2001, *ApJ*, 547, 172
 Wada, K. & Norman, C. A. 2002, *ApJ*, 566, L21 (WN02)
 Wada, K. & Tomisaka, K. 2005, *ApJ*, 619, 93
 Wada, K., Papadopoulos, P. P., & Spaans, M. 2009, *ApJ*, 702, 63
 Woo, J.-H., Kim, J. H., Imanishi, M., & Park, D. 2012, *AJ*, 143, 49
 Yamada, M., Wada, K., & Tomisaka, K. 2007, *ApJ*, 671, 73

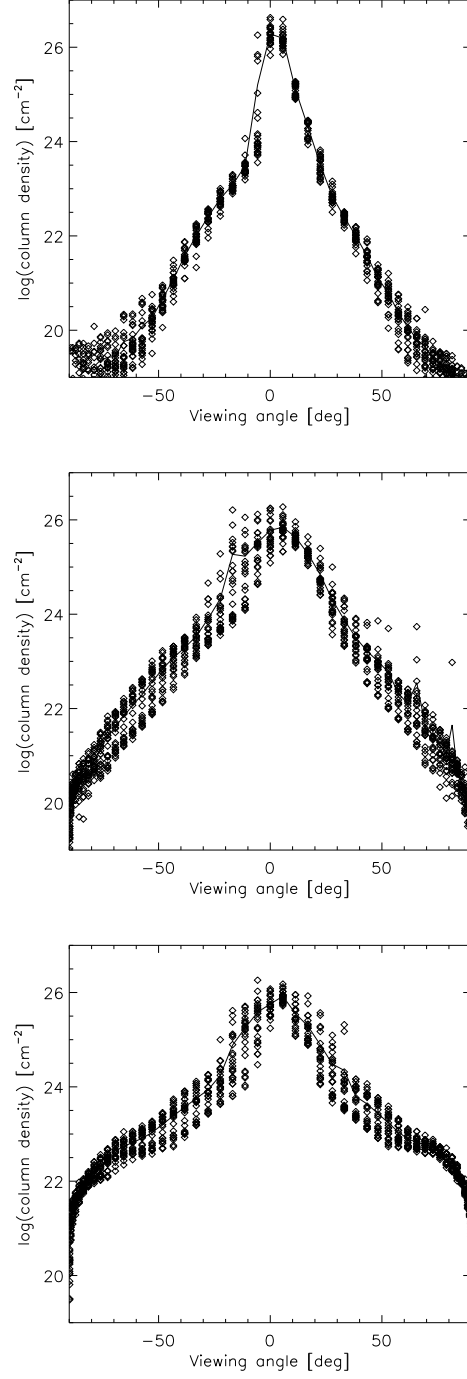


FIG. 8.— Total column density distribution as function of viewing angles (90° : pole-on view and 0° : edge-on view) and azimuthal angles. For each viewing angle, the column density is plotted for 50 azimuthal angles. The solid line indicates the azimuthal averaged column density for the viewing angles. (top) Before the radiation feedback is turned on ($t = 1.67$ Myr), (middle) $L_{AGN}/L_E = 0.01$ at $t = 4.55$ Myr, (bottom) $L_{AGN}/L_E = 0.1$ at $t = 4.68$ Myr.

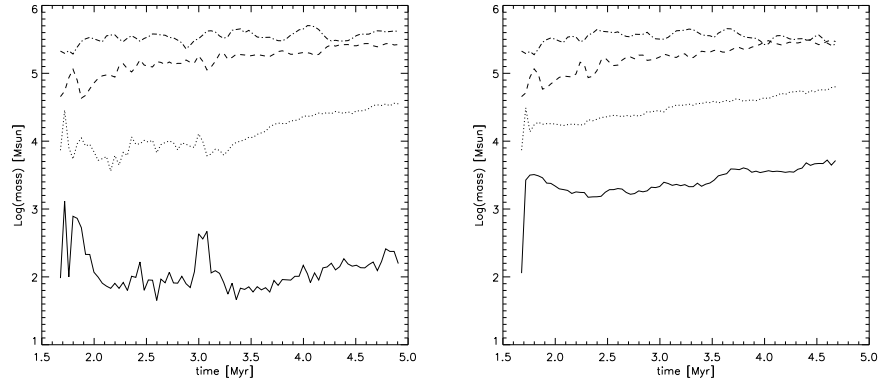


FIG. 9.— Evolution of radial mass. (left) model qi (Eddington ratio = 0.1) and (right) model qg (Eddington ratio = 0.01) for $r < 1.0$ pc (thick line), $1 \leq r < 2$ pc (dotted line), $2 \leq r < 4$ pc (dashed line), and $4 \leq r < 8$ pc (dot-dashed line).